

On the temperature dependent current transport mechanisms and barrier inhomogeneity in Au/SnO₂–PVA/n-Si Schottky barrier diodes

Ç. Bilkan¹ · Y. Badali² · S. Fotouhi-Shablou³ · Y. Azizian-Kalanderagh^{3,4} · Ş. Altındal⁵

Received: 12 April 2017 / Accepted: 24 July 2017
© Springer-Verlag GmbH Germany 2017

Abstract In this paper, we report the preparation and characterization of SnO₂–PVA nanocomposite film as interlayer for Schottky barrier diodes (SBDs). The possible current transport mechanisms (CTMs) of the prepared SBDs were investigated using the forward-bias current–voltage (I – V) characteristics in the temperature range of 80–400 K. The structure of nanocomposite film was characterized by an X-ray diffractometer (XRD) and the surface morphology was investigated using a Scanning Electron Microscopy (SEM) at room temperature. The values of ideality factor (n) and zero-bias barrier height ($\bar{\Phi}_{B0}$) showed variation with temperature, such that they changed from 19.10 to 3.77 and 0.190 to 0.844 eV, respectively. $\bar{\Phi}_{B0}$ – n , $\bar{\Phi}_{B0}$ – $q/2kT$, and n^{-1} – $q/2kT$ plots were drawn to get evidence to the Gaussian Distribution (GD) of the barrier height (BH). These plots revealed two distinct linear regions with different slopes for low temperatures (80–160 K) (LTs) and high temperatures (180–400 K) (HTs). This behavior is an evidence to the existence double GD of BHs which provides an average value for BH ($\bar{\Phi}_{B0}$) and a standard deviation (σ_s) for each region. The high

value of n especially at low temperatures was attributed to the existence of interlayer: interface states (N_{ss}) and barrier inhomogeneity at Au/n-Si interface. The values of $\bar{\Phi}_{B0}$ and σ_s were obtained from the intercept and slope of mentioned plots as 0.588 and 0.0768 V for LTs and 1.183 eV and 0.158 V for HTs, respectively. Moreover, the modified $\ln(I_s/T^2) - q^2\sigma_s^2/2k^2T^2$ vs q/kT plot also showed two linear regions. The values of $\bar{\Phi}_{B0}$ and effective Richardson constant (A^*) were extracted from the slope and intercept of this plot as 0.610 eV and 93.13 A/cm² K² for LTs and 1.235 eV and 114.65 A/cm² K² for HTs, respectively. The value of A^* for HTs is very close to the theoretical value (112 A/cm² K²) of n-type Si. Thus, the forward-bias I – V – T characteristics of Au/SnO₂–PVA/n-Si (SBDs) were successfully explained in terms of the thermionic-emission (TE) mechanism with a double GD of BHs.

1 Introduction

It is well known that metal–semiconductor (MS) contacts/structures are generally called MS-type Schottky barrier diodes (SBDs), since the first detailed work on this subject was reported by W. Schottky. When an interfacial insulator/oxide or polymer layer is inserted between metal and semiconductor by native growth or deposition, MS structure converts into MIS/MOS- or MPS-type structures or SBDs. These structures are important devices in the electronic and optoelectronic applications. In addition, these interfacial layers are greater than a few hundred Å, and these structures are called MIS/MOS or MPS capacitors. In this case, these structures can be stored more and more electric charges or energy. Besides, the use of interfacial layer at M/S interface prevents diffusion between metal and semiconductor and regulates the charge transitions

✉ Ç. Bilkan
cigdembilkan@gmail.com

¹ Department of Physics, Faculty of Sciences, Çankırı Karatekin University, Çankırı, Turkey

² Department of Advanced Technologies, Institute of Science and Technology, Gazi University, Ankara, Turkey

³ Department of Physics, University of Mohaghegh Ardabili, P. O. Box 179, Ardabil, Iran

⁴ Department of Engineering Sciences, Sabalan University of Advanced Technologies, Namin, Iran

⁵ Department of Physics, Faculty of Sciences, Gazi University, Ankara, Turkey

[1–4]. Owing to the technological importance of these devices, recently, researchers have focused on the development of SBDs with insulator, polymer, or ferroelectric interlayers in the form of MIS-, MPS-, and MFS-type SBDs [3–13]. They fabricated SBDs with various interlayer materials such as SiO_2 [3], BaTiO_3 [4], SnO_2 [5], $\text{Bi}_4\text{Ti}_3\text{O}_{12}$ [6], $\text{BaTiO}_3/\text{SrTiO}_3$ [7], Al_2O_3 [8], Al/CdS –PVA/p-Si [9], ZnO [10], graphene-doped PVA [11, 13], and Co_3O_4 –PVA [12] and then studied their electrical and dielectric properties using the forward and reverse biases I – V , capacitance/conductance–voltage (C – V and G/ω – V) measurements. Among them, organic/polymer interlayer materials grasped significant attention since their flexibility, low-cost production, low molecular weight, and large area of production compared to the conventional SiO_2 . Moreover, transition metal oxides or insulators such as titanium dioxide (TiO_2), zinc oxide (ZnO), and tin dioxide (SnO_2) have found utility in a wide range of applications such as sustainable clean energy, including solar cells, energy storage devices, and MIS-type SBDs due to their natural abundance, chemical inertness, and excellent photoelectric and electro-chemical properties [14–16]. In addition, TiO_2 , ZnO , and SnO_2 are materials with similar band structure and physical properties [17, 18]. Bulk SnO_2 is a well-known semiconductor material, and owing to its wide bandgap (3.6 eV) and mobility up to $240 \text{ cm}^2/(\text{Vs})$ [19], it was proposed for a wide range of important applications including as catalytic materials [20], gas sensors [21], rechargeable batteries [22], supercapacitors [23], and solar cells [19].

Mixed organic and inorganic nanostructure-based systems have been investigated as new compound materials for electronic and optoelectronic device applications [24]. Especially, hybrid films of polymers and semiconductor nanostructures are easy to fabricate and utilize as an interfacial layer in SBDs and have been reported before [25, 26].

The performance and quality of electronic devices such as MS-, MIS/MOS-, and MPS-type SBDs are dependent on many parameters such as the formation of interface layer and its thickness/homogeneity, process of surface fabrication, interface quality, the formation of BH between metal and semiconductor (M/S interface), density distribution of surface states (N_{ss}) located between interlayer and semiconductor, the magnitude of doping concentration atoms, series, and shunt resistances (R_s and R_{sh}), temperature, and applied bias voltage. Among them, the sample temperature and the form of BH at M/S interface are two parameters that have considerable effects on the possible transport/conduction mechanisms of these devices. It is well known that the electrical measurements only at room temperature cannot supply adequate information on the form of BH and conduction mechanism both. In this

respect, it is very important to investigate the current transport/conduction mechanisms in wide temperature and voltage range. In general, the semi-logarithmic I – V plots are linear in the intermediate voltage range ($3 \text{ kT}/q \leq V \leq 0.7 \text{ V}$ for Si-based diodes) with a good linear behaviour; however, it deviates from linearity at enough high forward biases due to effect of R_s and interfacial layer.

The assessment of the forward biases I – V data according to the standard thermionic-emission (TE) theory, usually, leads to an increase in $\bar{\Phi}_{\text{Bo}}$ and a decrease in n with increasing temperature [27–33]. This decrease in $\bar{\Phi}_{\text{Bo}}$ at low temperatures leads to a deviation from the linearity in the Richardson or Arrhenius plot. Contrary to the case at high temperatures, the charge carriers do not have enough energy to pass through the higher barriers at low temperatures. However, Schmitsdrof et al. [27] and Tung [28] showed the existence of nonuniform BH at M/S interface and they showed that the linear correlation between ideality factor and effective BH could be explained by lateral inhomogeneities of the BH. When the temperature and applied bias voltage start to increase, the apparent BH ($\bar{\Phi}_{\text{ap}}$) will begin to increase, but more and more charge carriers will gain energy to pass through higher barriers. In general, the formation of the barrier height between metal and semiconductor is not flat and it contains many lower barriers or patches at around mean single or double barrier heights ($\bar{\Phi}_{\text{Bo}}$) due to surface properties. While charge carriers do not have sufficient thermal energy to pass over mean BH at low temperatures, they can be easily pass through these patches/lower barriers and lead to an increase in ideality factor and decrease in zero-bias/apparent BH ($\bar{\Phi}_{\text{Bo}}/\bar{\Phi}_{\text{ap}}$). When the temperature starts to increase, more and more electrons/charges gain enough energy to overcome the mean or higher barriers [27, 34–41].

The study reported here is an example of the positioning of SnO_2 /PVA as the interface layer in fabricated Au/SnO_2 –PVA/n-Si (MPS)-type SBDs. To get more information on the current transport mechanisms (CTMs), the forward-bias current–voltage (I – V) characteristics were investigated in the wide range of temperature (80–400 K) and voltage [(-4 V)–(+6 V)] ranges. I – V – T characteristics of the prepared MPS structures were successfully interpreted by double-Gaussian distribution (DGD) of the BHs around a mean value of BH at Au/n-Si interface.

2 Experimental procedures

2.1 Materials and Instruments

Tin(II) chloride [(SnCl_2) , high-purity $\geq 99\%$] and sodium hydroxide (NaOH , purity $\geq 99\%$) were purchased from Merck. All of these chemical reagents were used without

purification. Then, morphology and structure investigations were performed using the LEO1430 VP scanning electron microscope (SEM) with 15 and 18 kV accelerating voltages. UV–visible absorption spectroscopy of the sample was characterized by a spectrometer, (Shimadzu, model 1650, Japan). The structural characterization was carried out by a Philips X Pert X-ray diffractometer with CuK α radiation ($\lambda = 1.54 \text{ \AA}$) employing a scanning step size of 0.02° , in 2θ range from 20° to 80° .

2.2 Synthesis and preparation

In a typical synthesis, for preparation of SnO₂ nanoparticles, 0.93 g tin(II) chloride (SnCl₂) and 0.16 g sodium hydroxide (NaOH) were dissolved in 5 ml distilled water, respectively. The sodium hydroxide solution was then added to the tin(II) chloride solution, and this mixture was placed under ultrasonic irradiation for 1 h at room temperature in open room. Ultrasonic irradiation was achieved using Dr. Heilscher high-intensity ultrasound processor, UP200H, Germany. After sonication, the solution was centrifuged for several times. The precipitation was washed with distilled water and then dried in a desiccator that connected to a vacuum pump. SnO₂–PVA nanocomposite film was prepared at room temperature by solution-casting method. For this purpose, aqueous solution of PVA was prepared by dissolving 5 g PVA in 100 cc-deionized water with vigorous stirring at 60°C . Then, 8 ml of the prepared solution was mixed with 2 cc aqueous of SnO₂, to prepare SnO₂–PVA nanocomposites.

2.3 The surface cleaning of n-Si wafers

Au/SnO₂–PVA/n-Si (MPS)-type SBDs were fabricated on the n-type (P-doped) single-crystal Si wafer with (100) float zone, 1–10 $\Omega\text{ cm}$ resistivity, 2" diameter, and 300 μm thickness. First, n-Si wafer was cleaned in RCA to remove organic residues. After that, it was rinsed in deionized water (DW) with a resistivity of 18 M $\Omega\text{ cm}$ and dried by high-pure nitrogen gas. Second, high-purity (99.999%) gold was deposited on whole backside of n-Si wafer in the metal evaporation system at about 10^{-6} Torr, and then, the wafer was annealed at about 550°C in nitrogen ambient for 5 min to get a low-resistivity ohmic back contact. Later, the prepared SnO₂–PVA solution was grown as nanocomposite film on the front of n-Si wafer by spin-coating method. Finally, high-purity Au rectifier/Schottky contacts were deposited on the SnO₂–PVA nanocomposite film with 1 mm diameter in the same high-vacuum thermal evaporation system. Thus, the fabrication processes of the Au/SnO₂–PVA/n-Si (MPS)-type SBDs were completed.

To conduct the I – V measurements, the samples were pasted onto the Cu holder with the help of silver paste, and

the upper Schottky contacts were connected using silver paste and thin Cu wires. Current–voltage measurements were performed with a Keithley 2400 source meter, a microcomputer, and an IEEE-488 AC/DC converter card. Measurements were conducted in the VPF-475 cryostat for temperature control and further reduction of external influences and noises. The schematic representation of the MPS structure is shown in Fig. 1.

3 Results and discussion

3.1 Structural and optical analysis

The X-ray diffraction (XRD) pattern of SnO₂ nanoparticles powder is shown in Fig. 2. The peaks at 2θ values of 26.6° , 33.8° , 37.9° , 51.8° , and 54.7° can be associated with (110), (101), (200), (211), and (220), respectively. The SnO₂ product shows tetragonal structure. The average particle size (D) was determined using the Scherer's equation:

$$D = K\lambda / (\beta \cos \theta), \quad (1)$$

where λ is the wavelength of the X-ray (1.54 \AA). θ is the angle of the considered peak, β is a full-width at half-maximum (FWHM) of the peak, and K is a constant close to unity. Values for the coefficient K depend on factors such as the geometry of the crystallite and unfortunately are not always consistently used in the literature. Nanocrystallite sizes have been calculated from the line broadening of XRD diffraction peaks according to the Scherer formula and are listed in Table 1. All calculations confirm that the structures are nanocrystalline in nature with average size below 40 nm.

The UV–Visible absorption spectrum of the structure is shown in Fig. 3. The UV–Visible absorption spectrum of the sonochemically prepared SnO₂ nanostructures has a large bandgap (about 4 eV) due to the quantum confinement effect and the blue shift in bandgap of nanostructure is related to the confinement of charge carriers in very small nanosized SnO₂.

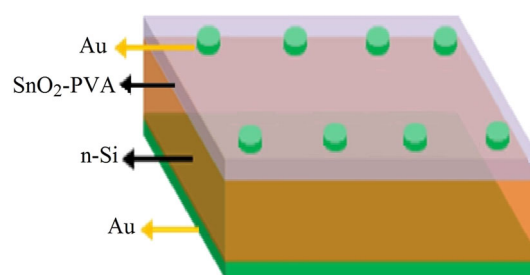


Fig. 1 Schematic representation of MPS-type SBDs

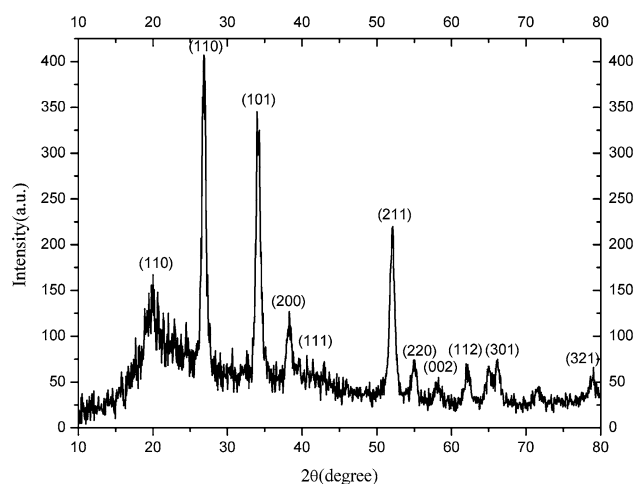


Fig. 2 X-ray diffraction pattern of SnO₂ nanopowders

Table 1 Nanocrystallite size calculated from XRD pattern of SnO₂ nanopowders

No.	Pos [2θ°]	FWHM [2θ°]	Nanocrystallite size (nm)
1	19.7	1.18	7.19
2	26.7	0.24	37.1
3	34.0	0.29	30.1
4	38.3	0.71	12.6
5	52.1	0.35	26.7
6	55.0	0.71	13.3
7	58.2	0.94	9.91
8	62.1	0.47	20.6

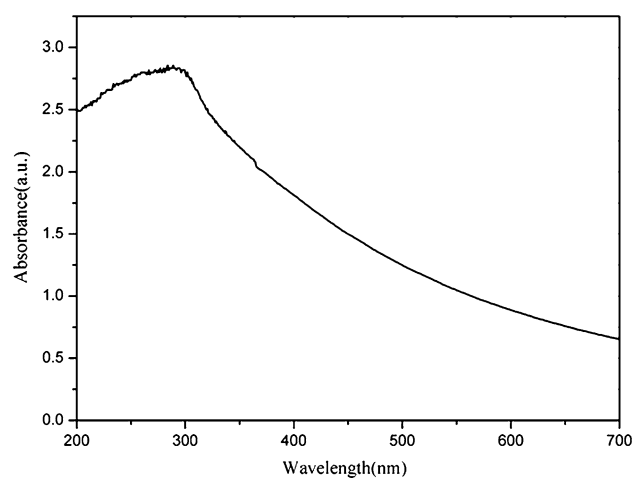


Fig. 3 UV-Visible spectrum of SnO₂ nanostructures

3.2 Morphological studies

The surface morphologies of the SnO₂-PVA composite were characterized by SEMs. Figure 4 illustrates the SEM images of

the sample at magnifications of (a) 10 and (b) 30 k, respectively. As shown in Fig. 4, the SEM images illustrate that the nearly smooth surface is composed and nanoparticles are spread across the PVA polymer in the form of polydispersive nanoclusters.

3.3 Current-voltage-temperature (*I-V-T*) characteristics

Figure 5 shows typical semi-logarithmic forward- and reverse-bias *I-V* characteristics of the Au/SnO₂-PVA/n-Si (MPS)-type SBDs in a wide temperature range (80–400 K) by 20 K steps. It is seen that the current has an exponential increase in the forward bias and weaker voltage dependence in the reverse bias regions for all temperatures. To determine whether or not MPS-type SBD has an ideal diode behavior, its experimental forward-bias *I-V* characteristics at low and intermediate voltages ($V \geq 3 \text{ kT/q}$) were analyzed on the basis of thermionic-emission (TE) theory [1, 2]:

$$I = I_0 \left[\exp\left(\frac{q(V - IR_s)}{nkT}\right) - 1 \right]. \quad (2)$$

In Eq. 2, I_0 is the reverse-saturation current, V is the voltage applied on the diode, k is the Boltzmann constant, the term of IR_s is the voltage drops on the series resistance

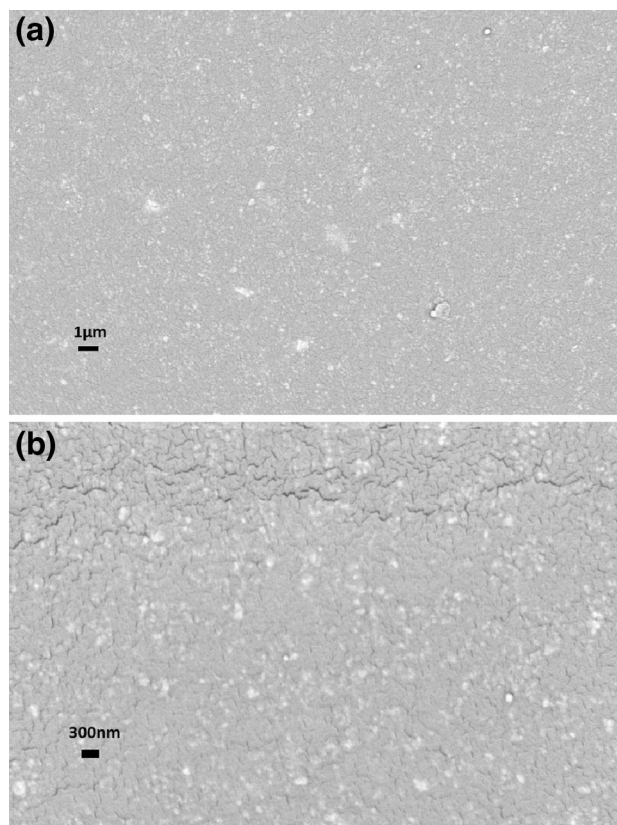


Fig. 4 SEM images of SnO₂-PVA nanocomposites at different magnifications **a** 1 μm and **b** 300 nm

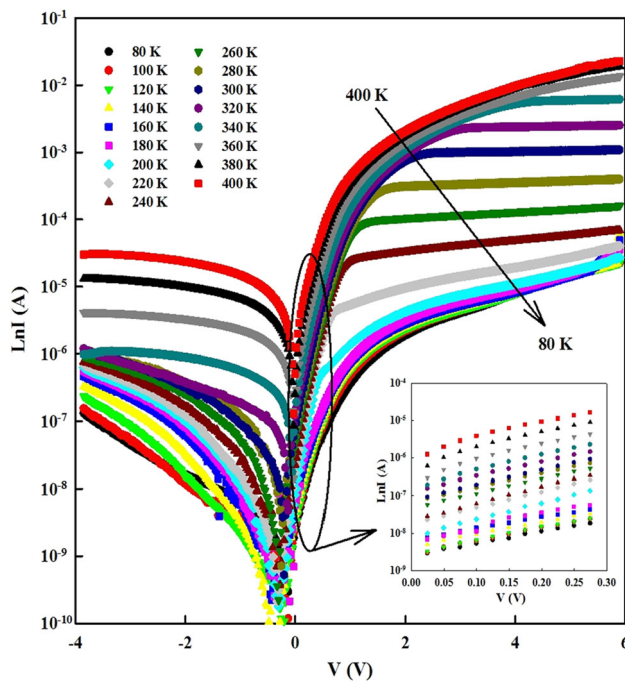


Fig. 5 Semi-logarithmic current–voltage characteristics with temperature for Au/SnO₂–PVA/n-Si (MPS)-type SBD

(R_s) of the diode, and n is the ideality factor [1]. Inset of Fig. 5 shows that $\ln I$ – V plot in the forward-bias region has a good linear region for all temperatures ($3 \text{ kT}/q \leq V \leq 0.3 \text{ V}$) with different slopes. The values of I_0 in Eq. 2 were obtained from the intercept of the linear part $\ln I$ – V plot for all temperatures. I_0 is expressed as [1, 2]

$$I_0 = AA^*T^2 \exp\left(-\frac{q}{kT} \Phi_{B0}\right), \quad (3)$$

where A^* is the Richardson constant ($112 \text{ A/cm}^2 \text{ K}^2$ for n-Si), A is the Schottky contact area, T is the absolute temperature in K, and Φ_{B0} is the zero-bias barrier height. Similarly, the values of n can be obtained from the slope of the linear part of $\ln I$ – V plot for all temperatures using the following equation [2, 41]:

$$n = \frac{q}{kT} \frac{dV}{d(\ln I)}. \quad (4)$$

Φ_{B0} values were obtained using the extracted I_0 values and theoretical value of A^* in the following equation for all temperatures [1, 41]:

$$\Phi_{B0} = \frac{kT}{q} \ln\left(\frac{AA^*T^2}{I_0}\right). \quad (5)$$

The experimental values of I_0 , n , and Φ_{B0} are represented in Table 1 for all temperatures, such that they changed from $2.58 \times 10^{-9} \text{ A}$, 19.10, and 0.19 eV (at 80 K) to $1.34 \times 10^{-6} \text{ A}$, 3.77, and 0.844 eV (at 400 K), respectively. The changes in n and Φ_{B0} with temperature are also

given in Fig. 6. Table 2 and Fig. 6 clearly show that all of these parameters (I_0 , n , and Φ_{B0}) are strong functions of temperature. It is also seen that the value of Φ_{B0} is decreased and the value of n is increased with decreasing temperature. Such a temperature dependence of the n and Φ_{B0} suggests that there exists deviation from the ideal TE theory.

This positive temperature coefficient of BH does not obey negative temperature coefficient of forbidden band-gap of Si ($\alpha = dE_g/dT = 4.73 \times 10^{-4} \text{ eV K}^{-1}$) or an ideal diode. Therefore, the change in n and Φ_{B0} with temperature for the fabricated Au/SnO₂–PVA/n-Si (MPS)-type SBDs could be associated with the existence of a spatially inhomogeneous BH which consist of lower and higher barriers or patches with different areas [8, 11, 28–31] due to the poor interface quality, spatial density distribution surface states (N_{ss}) and dislocations, the inhomogeneities in the interfacial insulator or polymer layer, and non-uniformity of the doping concentration atoms. Very recently, Güçlü et al. [8] and Yerişkin et al. [11] have reported similar results. Due to the existence of low and high patches along BH, Sullivan et al. [33] and Tung [28] modified TE theory. On the other hand, Song et al. [29] proposed another model for current transport at low and intermediate temperatures by considering a Gaussian distribution (GD) of BH. They assumed that the M/S interface of an SBD comprises many parallel SBDs.

In the MS-type SBDs with and without interfacial layer, various current transport mechanisms, such as thermionic emission (TE), thermionic-field emission (TFE), and field emission (FE), may dominate the others at a certain temperature and at voltage regions. Tunneling through the barrier is consistent with TFE and FE mechanisms. On the other hand, a simultaneous contribution from two or more mechanisms could also be possible. Among the possible

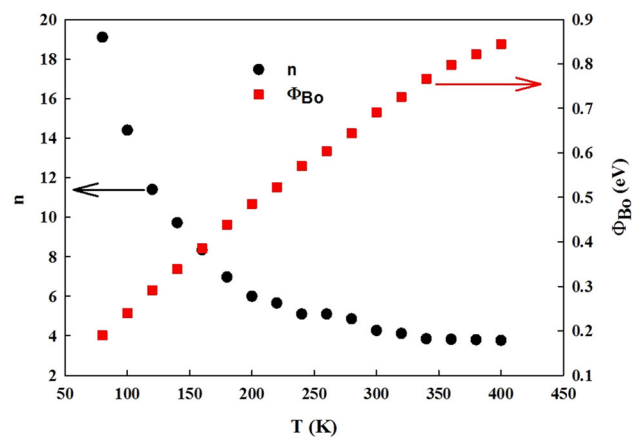


Fig. 6 Φ_{B0} and n vs T characteristics for Au/SnO₂–PVA/n-Si (MPS)-type SBD

Table 2 Change in I_o , n , and $\bar{\Phi}_{Bo}$ values with temperature for Au/SnO₂-PVA/n-Si (MPS) SBD

T (K)	I_o (A)	n	$\bar{\Phi}_{Bo}$ (eV)	$\bar{\Phi}_{Bef}$ (eV)	nT (K)
80	2.58×10^{-9}	19.10	0.190	0.988	1528.0
100	2.89×10^{-9}	14.40	0.240	0.972	1440.0
120	3.02×10^{-9}	11.40	0.291	0.961	1368.0
140	4.56×10^{-9}	9.72	0.339	0.944	1360.8
160	6.87×10^{-9}	8.35	0.385	0.910	1336.0
180	6.02×10^{-9}	6.97	0.439	0.895	1254.6
200	8.44×10^{-9}	6.00	0.485	0.843	1200.0
220	1.84×10^{-8}	5.66	0.523	0.811	1245.2
240	2.22×10^{-8}	5.10	0.570	0.796	1224.0
260	4.84×10^{-8}	5.100	0.604	0.792	1326.7
280	7.23×10^{-8}	4.86	0.644	0.782	1360.5
300	7.89×10^{-8}	4.27	0.691	0.742	1280.9
320	1.35×10^{-7}	4.12	0.726	0.717	1318.9
340	1.80×10^{-7}	3.85	0.767	0.693	1309.0
360	3.15×10^{-7}	3.82	0.798	0.676	1375.2
380	6.65×10^{-7}	3.80	0.821	0.630	1444.0
400	1.34×10^{-6}	3.77	0.844	0.580	1508.0

mechanisms, TFE and FE are particularly important at low temperatures and high-doping concentration of donor or acceptor atoms. The increase in $\bar{\Phi}_{Bo}$ and decrease in n with increasing temperature point out a deviation which may occur at low temperatures due to high number of doping concentration atoms [1, 2, 40–42]. In this case, the relationship between current and voltage can be expressed as follows [1, 2, 42]:

$$I = I_{\text{tun}} \left[\exp \left(\frac{q(V - IR_s)}{E_o} \right) - 1 \right] \quad (6)$$

with

$$n_{\text{tun}} = \frac{E_{oo}}{kT} \coth \left(\frac{E_{oo}}{kT} \right) = \frac{E_o}{kT}. \quad (7)$$

In Eq. 7, E_{oo} is the characteristic tunneling energy, which is related to the tunnel effect transmission probability:

$$E_{oo} = \frac{h}{4\pi} \left(\frac{N_D}{m_e^* \epsilon_s} \right)^{1/2}, \quad (8)$$

where m_e^* ($=0.98 m_o$) is the effective mass of electron, ϵ_s ($=11.8\epsilon_o$) is the permittivity of Si, and ϵ_o ($=8.85 \times 10^{-12}$ F/m) is the permittivity of free space. Thus, the value of E_{oo} was found as 0.36 meV at room temperature. It is well known that the tunneling mechanism, which is including TFE and FE theories, should be dominant when $E_{oo} \approx kT/q$ and $E_{oo} \ll kT/q$, respectively. In this case, the TFE and FE theories are both invalid. Figure 7 shows E_o ($=nkT/q$) vs

kT/q plot for the Au/SnO₂-PVA/n-Si (MPS)-type SBD in the temperature range of 80–400 K. The value of E_o was calculated to be 118 meV corresponding to a doping concentration of $4.70 \times 10^{20} \text{ cm}^{-3}$.

The obtained experimental value of E_o is not close to the theoretical value of 0.36 meV calculated from the donor concentration (N_D) of n-Si. To explain these abnormal forward-bias I - V characteristics in the fabricated Au/SnO₂-PVA/n-Si (MPS)-type SBDs, a spatial distribution of the BH by a GD $P(\bar{\Phi}_{Bo})$ with a mean value of $\bar{\Phi}_{Bo}$ and standard deviation σ_o can be expressed as [27–31]

$$P(\Phi_{Bo}) = \frac{1}{\sigma_o \sqrt{2\pi}} \exp \left[-\frac{(\Phi_{Bo} - \bar{\Phi}_{Bo})^2}{2\sigma_o^2} \right]. \quad (9)$$

In this case, the total current across the BH in the forward-bias region can be expressed by the following equation.

Thus, by introducing $P(\bar{\Phi}_{Bo})$ and $I(\bar{\Phi}_{Bo})$ from Eqs. (9) and (10), the current of SBD with the modified barrier will be in the following form:

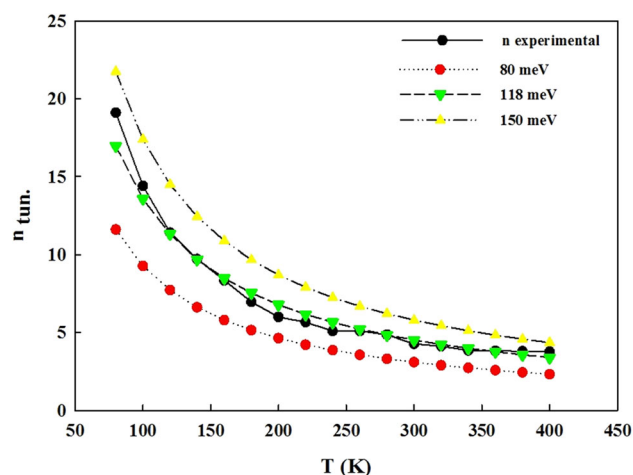
$$I(V) = AA^* T^2 \exp \times \left[-\frac{q}{kT} \left(\bar{\Phi}_{Bo} - \frac{q\sigma^2}{2kT} \right) \right] \left[\exp \left(\frac{q(V - IR_s)}{n_{ap} kT} \right) - 1 \right]. \quad (10)$$

The apparent BH ($\bar{\Phi}_{ap}$) and apparent ideality factor (n_{ap}) are given [27–31]:

$$\Phi_{ap} = \left[\bar{\Phi}_{Bo}(T=0) - \frac{q\sigma^2}{2kT} \right] \quad (11)$$

$$\left(\frac{1}{n_{ap}} - 1 \right) = \rho_2 - \left(\frac{q\rho_3}{2kT} \right). \quad (12)$$

In Eq. 12, ρ_1 and ρ_3 are the voltage coefficients, which may depend on temperature, and they quantify the voltage

**Fig. 7** Variation of ideality factor with temperature for the Au/SnO₂-PVA/n-Si (MPS)-type SBD

deformation of barrier height distribution [30, 31]. According to the Gaussian distribution model for BHs, the modified BH and standard deviation (σ_o) have linear dependence on Gaussian parameters, which are bias dependent. Therefore, another way to obtain the more reliable and accurate value of BH or possible conduction mechanisms is to use the values of BH and n in Eqs. 9–12 and to draw the modified Richardson plot in the whole temperature range.

$\bar{\Phi}_{Bo}$ vs n plot (Fig. 8) was drawn to determine if there is a linear relationship between these parameters. It is seen in Fig. 8 that there is a good linear relation between $\bar{\Phi}_{Bo}$ and n . This plot has two distinct linear regions with different slopes which correspond to the LTs and HTs ranges. The mean value of BH ($\bar{\Phi}_{Bo}$) ($n = 1$ for ideal case) was extracted as 0.334 eV for LTs and 1.142 eV for HTs. The decrease in $\bar{\Phi}_{Bo}$ and increase in n are also a result of the existence of inhomogeneous BH at M/S interface. Therefore, for the purpose of obtaining an evidence on the GD of BHs, both $\bar{\Phi}_{Bo}$ vs $q/2kT$ and $(n^{-1}-1)$ vs $q/2kT$ plots were drawn and is given in Figs. 9 and 10, respectively. Clearly, both these plots have two linear regions at low (80–160 K) and high (180–400 K) temperatures. Such a behavior of these two plots provides evidence the double GD of BH at M/S interface. Thus, according to Eq. 11, the intercept and slope of Fig. 9 yield $\bar{\Phi}_{Bo}$ and σ_o as 0.588 eV and 0.0768 V for LTs and 1.183 eV and 0.158 V for HTs, respectively. The value of σ_o is a measure of the barrier homogeneity. Therefore, low value of σ_o indicates homogeneous BH distribution, whereas high value of it suggests inhomogeneous BH distribution. In other words, many patches or low barriers may be located around mean BH, and in this case, the current passing through the diode is often governed by these low patches/barriers, and therefore, it leads to an increase in the ideality factor especially at low temperatures.

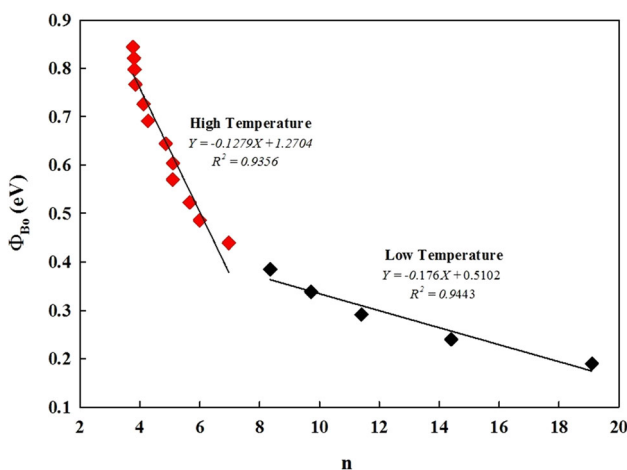


Fig. 8 $\bar{\Phi}_{Bo}$ vs n plots for Au/SnO₂-PVA/n-Si (MPS)-type SBD

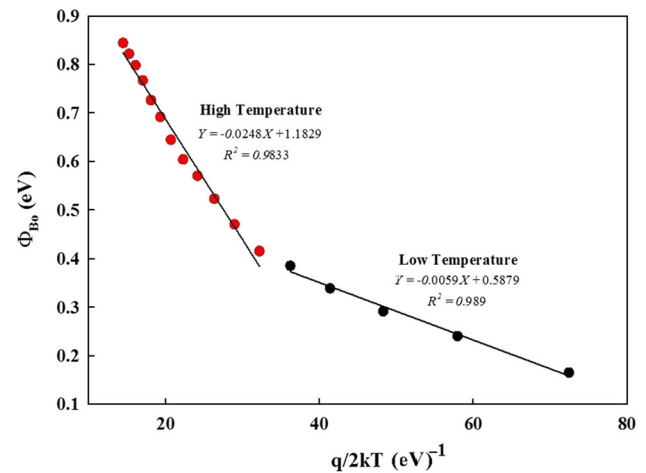


Fig. 9 $\bar{\Phi}_{Bo}$ vs $q/2kT$ plots for Au/SnO₂-PVA/n-Si (MPS)-type SBD

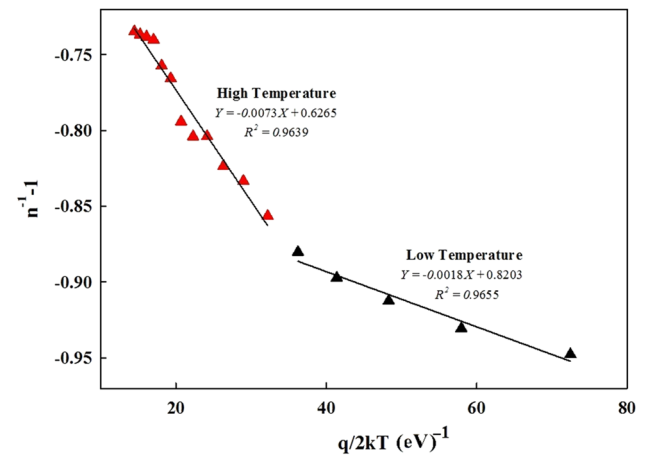


Fig. 10 $n^{-1}-1$ vs $q/2kT$ plots for Au/SnO₂-PVA/n-Si (MPS)-type SBD

In addition, $(n^{-1}-1)$ vs $q/2kT$ plot for the Au/SnO₂-PVA/n-Si (MPS)-type SBD is given in Fig. 10 to obtain voltage-dependent coefficients (σ_2 and σ_3). This plot also revealed two distinct linear regions with different slopes in the same temperature range. Utilizing Eq. 12, the values of ρ_2 and ρ_3 were extracted as -0.8203 and -0.0018 V for LTs and -0.6265 and -0.0073 V for HTs, respectively. Figures 8, 9, 10 suggest that $\bar{\Phi}_{Bo}$ and n , both, are quite dependent on temperature and voltage. These experimental results for the Au/SnO₂-PVA/n-Si (MPS)-type SBDs indicate that there are two different CTMs or two different BHs ($\bar{\Phi}_{Bo}$) in the temperature range of 80–400 K.

The high values of n even at high temperatures can be explained by the barrier inhomogeneity rather than the existence of (SnO₂-PVA) interfacial layer, image force lowering, recombination current, and N_{ss} [42–44]. At low temperatures, the charge carriers (electrons and holes) are able to surmount the lower barriers/patches and this leads

to higher values of n [28, 30, 31], but at high temperatures, more and more electrons gain sufficient energy to overcome higher barriers.

Another way to determine the value of BH is to draw the conventional Richardson plot [$\ln(I_0/T^2)$ vs q/kT]. The value of A^* and BH or activation energy (E_a) can be obtained from the intercept point and slope of this plot. Therefore, the [$\ln(I_0/T^2)$ vs q/kT] plot was drawn and is given in Fig. 11. It is seen in the figure that the Richardson plot deviates from the linearity especially at low temperatures. In addition, the values of A^* and BH were extracted as 78 meV and 2.9×10^{-9} A/cm² K², respectively. It is clear that especially, the value of A^* is 3.9×10^{10} times lower than their theoretical value (112 A/cm² K²), and therefore, this result shows that there is a deviation from the TE theory. Previously, the experimental data showed that there is an increase in $\bar{\Phi}_{Bo}$, whereas a decrease in n as the temperature is increased. This finding also provided an evidence to deviation from the TE theory, such that n values suggested that the TFE and FE could be possible current conduction mechanisms at intermediate- and low-temperature ranges, respectively [45–47]. It is well known that the FE and TFE theories require a change in the tunneling current parameter E_o ($=nkT/q$) with temperature [3, 44].

Conventional Richardson plot [$\ln(I_0/T^2)$ vs q/kT] deviated from the linearity especially at low temperatures and yields very low Richardson constant (A^*) and BH due to barrier inhomogeneities between metal and semiconductor. Therefore, the more reliable value of the A^* and mean value of BH were calculated by employing modified Richardson plot [$\ln(I_s/T^2) - q^2\sigma_s^2/2k^2T^2$ vs q/kT], as given in Fig. 12. Like the previous plots, modified Richardson plot also revealed two linear regions for low- and high-temperature regions. The values of $\bar{\Phi}_{Bo}$ and effective

Richardson constant (A^*) were extracted from the slope and intercept of these plots as 0.610 eV and 93.13 A/cm² K² at LTs and 1.235 eV and 114.65 A/cm² K² at HTs, respectively. The value of A^* for HTs is very close to its theoretical value (112 A/cm² K²) for n-type Si. Thus, the forward-bias I – V – T characteristics in MPS-type SBD were successfully explained in terms of the thermionic-emission (TE) mechanism with a double GD of BHs. These results could be attributed to the greater inhomogeneity at the Schottky interface and it leads to the reduction of the intimate effective area that represents only a small fraction of the geometric area.

4 Conclusion

Temperature dependence of electrical characteristics of the Au/SnO₂–PVA/n-Si (MPS)-type SBDs was investigated using the forward-bias I – V measurements in the wide temperature range of 80–400 K to get detailed information on the BH and possible current transport/conduction mechanisms. Obtained experimental results showed that with increasing temperature, the value of $\bar{\Phi}_{Bo}$ increased, whereas the value of n decreased. This anomalous behavior of BH and high values of n at low temperatures could be associated with the nature of inhomogeneous BH which consists of low and high barriers or patches between metal and semiconductor. The plots of $\bar{\Phi}_{Bo}$ – n , $\bar{\Phi}_{Bo}$ – $q/2kT$, and n^{-1} – $q/2kT$ were drawn to explore evidence to the GD of the BH. These plots exhibited two distinct linear regions with different slopes that correspond to the low (80–160 K) and high (180–400 K) temperature ranges. Therefore, it was found that the conduction mechanism is quite different at low and high temperatures. Such a behavior of these plots provides an evidence to the existence of a double GD of

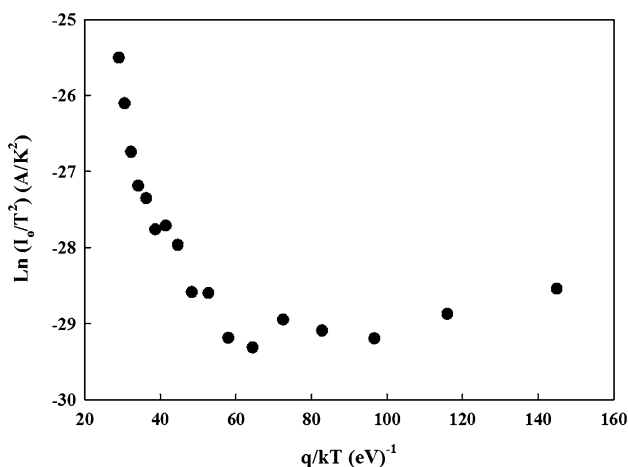


Fig. 11 [$\ln(I_0/T^2)$ vs q/kT] plot for Au/SnO₂–PVA/n-Si (MPS)-type SBD

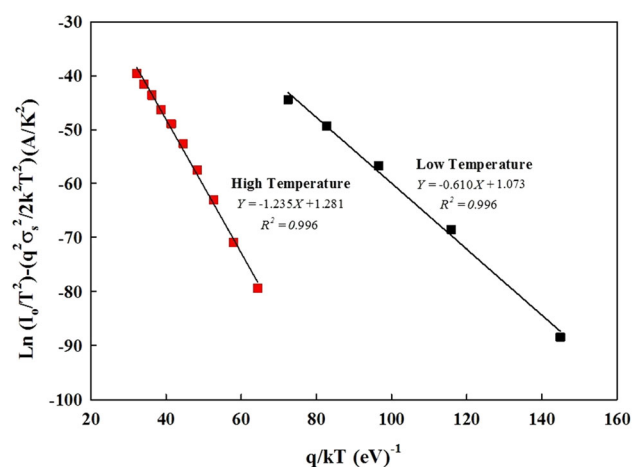


Fig. 12 Modified Richardson plot for the Au/SnO₂–PVA/n-Si (MPS)-type SBD

BHs for the Au/SnO₂-PVA/n-Si-type SBDs. Moreover, the values of $\bar{\Phi}_{B_0}$ and σ_0 were obtained as 0.588 eV and 0.0768 V for LTs and 1.183 eV and 0.158 V for HTs, respectively. In addition, the values of $\bar{\Phi}_{B_0}$ and effective Richardson constant (A^*) were extracted as 0.610 eV and 93.13 A/cm² K² at LTs and 1.183 eV and 114.65 A/cm² K² at HTs, respectively. It is clear that this value of A^* especially for HTs is very close to its theoretical value (112 A/cm² K²) for n-type Si. Thus, the forward-bias I - V - T characteristics of the fabricated Au/SnO₂-PVA/n-Si (MPS)-type SBDs were successfully explained in terms of the TE theory with a double GD of BHs.

References

1. S.M. Sze, *Physics of semiconductor devices*, 2nd edn. (Wiley, New York, 1981)
2. E.H. Rhoderick, R.H. Williams, *Metal-semiconductor contacts* (Clarendon, Oxford, 1988)
3. V.R. Reddy, M.S. Pratap Reddy, B.P. Lakshmi, A. Ashok Kumar, Electrical characterization of Au/n-GaN metal-semiconductor and Au/SiO₂/n-GaN metal-insulator-semiconductor structures. *J. Alloy Compd.* **509**, 8001 (2011)
4. V.R. Reddy, V. Manjunath, V. Janardhanam, Y.-H. Kil, C.-J. Choi, Electrical properties and current transport mechanisms of the Au/n-GaN Schottky structure with solution-processed high-k BaTiO₃ interlayer. *J. Electron. Mater.* **43**, 3499 (2014)
5. M. Yıldırım, M. Gökçen, Controlling the electrical characteristics of Au/n-Si structures by interfacial insulator layer. *Mat. Sci. Semicond. Proc.* **15**, 406 (2012)
6. Ş. Altındal, F. Parlaktürk, A. Tataroğlu, M. Parlak, S.N. Sarımasov, A.A. Agasiev, The temperature profile and bias dependent series resistance of Au/Bi₄Ti₃O₁₂/SiO₂/n-Si (MFIS) structures. *Vacuum* **82**, 1246 (2008)
7. G. Panomsuwan, O. Takai, N. Saito, Enhanced memory window of Au/BaTiO₃/SrTiO₃/Si (001) MFIS structure with high c-axis orientation for non-volatile memory applications. *Appl. Phys. A* **108**, 337 (2012)
8. Ç.Ş. Güçlü, A.F. Özdemir, Ş. Altındal, Double exponential I - V characteristics and double Gaussian distribution of barrier heights in (Au/Ti)/Al₂O₃/n-GaAs (MIS)-type Schottky barrier diodes in wide temperature range. *Appl. Phys. A* **122**, 1032 (2016)
9. G. Ersöz, İ. Yücedağ, Y. Azizian-Kalandaragh, İ. Orak, Ş. Altındal, Investigation of electrical characteristics in Al/CdS-PVA/p-Si (MPS) structures using impedance spectroscopy method. *IEEE T Electron. Dev* **63**, 2948 (2016)
10. S.O. Tan, H. Uslu Tecimer, O. Çiçek, H. Tecimer, İ. Orak, Ş. Altındal, Electrical characterizations of Au/ZnO/n-GaAs Schottky diodes under distinct illumination intensities. *J. Mater. Sci. Mater. El* **27**, 8340–8347 (2016)
11. S. Altındal Yerişkin, M. Balbaşı, S. Demirezen, Temperature and voltage dependence of barrier height and ideality factor in Au/0.07 graphene-doped PVA/n-Si structures. *Indian J. Phys.* **91**, 421–430 (2017)
12. Ç. Bilkan, Y. Azizian-Kalandaragh, Ş. Altındal, R. Shokrani-Havigh, Frequency and voltage dependence dielectric properties, ac electrical conductivity and electric modulus profiles in Al/Co₃O₄-PVA/p-Si structures. *Phys. B* **500**, 154 (2016)
13. S. Altındal Yerişkin, M. Balbaşı, A. Tataroğlu, Frequency and voltage dependence of dielectric properties, complex electric modulus, and electrical conductivity in Au/7% graphene doped-PVA/n-Si (MPS) structures. *J. Appl. Polym. Sci.* **133**, 43827 (2016)
14. E.J.W. Crossland, N. Noel, V. Sivaram, T. Leijtens, J.A. Alexander-Webber, H.J. Snaith, Mesoporous TiO₂ single crystals delivering enhanced mobility and optoelectronic device performance. *Nature* **495**, 215 (2013)
15. Y. Izumi, Recent advances in the photocatalytic conversion of carbon dioxide to fuels with water and/or hydrogen using solar energy and beyond. *Coord. Chem. Rev.* **257**, 171 (2013)
16. J. Schneider, M. Matsuoka, M. Takeuchi, J. Zhang, Y. Horiuchi, M. Anpo, D.W. Bahnemann, Understanding TiO₂ photocatalysis: mechanisms and materials. *Chem. Rev.* **114**, 9919 (2014)
17. J. Xu, Z.H. Chen, J.A. Zapien, C.S. Lee, W.J. Zhang, Surface engineering of ZnO nanostructures for semiconductor-sensitized solar cells. *Adv. Mater.* **26**, 5337 (2014)
18. J. Tian, G. Cao, Design, fabrication and modification of metal oxide semiconductor for improving conversion efficiency of excitonic solar cells. *Coord. Chem. Rev.* **320–321**, 193–215 (2016)
19. H.J. Snaith, C. Ducati, SnO₂-Based Dye-Sensitized Hybrid Solar Cells Exhibiting Near Unity Absorbed Photon-to-Electron Conversion Efficiency. *Nano Lett.* **10**, 1259–1265 (2010)
20. Y. Han, X. Wu, Y. Ma, L. Gong, F. Qu, H. Fan, Porous SnO₂ nanowire bundles for photocatalyst and Li ion battery applications. *CrystEngComm* **13**, 3506–3510 (2011)
21. J. Zhang, J. Guo, H. Xu, B. Cao, Reactive-template fabrication of porous SnO₂ nanotubes and their remarkable gasensing performance. *ACS Appl. Mater. Interface* **5**, 7893–7898 (2013)
22. P. Meduri, C. Pendyala, V. Kumar, G.U. Sumanasekera, M.K. Sunkara, Hybrid tin oxide nanowires as stable and high capacity anodes for li-ion batteries. *Nano Lett.* **9**, 612–616 (2009)
23. S.N. Pusawale, P.R. Deshmukh, C.D. Lokhande, Chemical synthesis of nanocrystalline SnO₂ thin films for supercapacitor application. *Appl. Surf. Sci.* **257**, 9498–9502 (2011)
24. M. Eckle, G. Decher, Tuning the performance of layer-by-layer assembled organic light emitting diodes by controlling the position of isolating clay barrier sheets. *Nano Lett.* **1**, 45–49 (2001)
25. Ç. Bilkan, Ş. Altındal, Y. Azizian-Kalandaragh, Investigation of frequency and voltage dependence surface states and series resistance profiles using admittance measurements in Al/p-Si with Co₃O₄-PVA interlayer structures. *Phys. B* **515**, 28–33 (2017)
26. Y. Azizian-Kalandaragh, F. Sedaghatdoust-Bodagh, E. Alizadeh-Gheshlaghi, A. Khodayari, Characterization of some electrical properties of CdS-Gelatin nanocomposites using hall measurement technique. *J. Nanoelectron. Optoelectron.* **12**, 231–235 (2017)
27. R.F. Schmitsdorf, T.U. Kampen, W. Mönch, Explanation of the linear correlation between barrier heights and ideality factors of real metal-semiconductor contacts by laterally nonuniform Schottky barriers. *J. Vac. Sci. Technol. B* **15**, 1221 (1997)
28. R.T. Tung, Recent advances in Schottky barrier concepts. *Mat. Sci. Eng. R* **35**, 1 (2001)
29. Y.P. Song, R.L. Van Meirhaeghe, W.H. Laflere, F. Cardon, On the difference in apparent barrier height as obtained from capacitance-voltage and current-voltage-temperature measurements on Al/p-InP Schottky barriers. *Solid State Electron.* **29**, 633 (1986)
30. J.H. Werner, H.H. Güttler, Barrier inhomogeneities at Schottky contacts. *J. Appl. Phys.* **69**, 1522 (1991)
31. M.K. Hudait, S.B. Krupanidhi, Interface states density distribution in Au/n-GaAs Schottky diodes on n-Ge and n-GaAs substrates. *Mat. Sci. Eng. B* **87**, 141 (2001)
32. A. Kaya, S. Demirezen, H. Tecimer, Ş. Altındal, Temperature and voltage effect on barrier height and ideality factor in Au/PVC + TCNQ/p-Si structures. *Adv. Polym. Technol.* **33**, 21442 (2014)

33. J.P. Sulvian, R.T. Tung, M.R. Pinto, W.R. Graham, Electron transport of inhomogeneous Schottky barriers: a numerical study. *J. Appl. Phys.* **70**, 7403 (1991)
34. L. Huang, Barrier inhomogeneities of platinum contacts to 4H-SiC. *Superlattice Microstruct.* **100**, 648–655 (2016)
35. W. Mönch, On the band-structure lineup at Schottky contacts and semiconductor heterostructures. *Mat. Sci. Semicond. Proc.* **28**, 2–12 (2014)
36. R. Singh, P. Sharma, M.A. Khan, V. Garg, V. Awasthi, A. Kranti, S. Mukherjee, Investigation of barrier inhomogeneities and interface state density in Au/MgZnO: Ga Schottky contact. *J. Phys. D Appl. Phys.* **49**, 445303 (2016)
37. Z. Khurelbaatar, M.-S. Kang, K.-H. Shim, H.-J. Yun, J. Lee, H. Hong, S.-Y. Chang, S.-N. Lee, C.-J. Choi, Temperature dependent current-voltage characteristics of Au/n-type Ge Schottky barrier diodes with graphene interlayer. *J. Alloys Compd.* **650**, 658–663 (2015)
38. A. Chatterjee, S.K. Khamari, V.K. Dixit, S.M. Oak, T.K. Sharma, Dislocation-assisted tunnelling of charge carriers across the Schottky barrier on the hydride vapour phase epitaxy grown GaN. *J. Appl. Phys.* **118**, 175703 (2015)
39. I. Jyothi, V. Janardhanam, H. Hong, C.-J. Choi, Current-voltage and capacitance-voltage characteristics of Al Schottky contacts to strained Si-on-insulator in the wide temperature range. *Mat. Sci. Semicond. Proc.* **39**, 390–399 (2015)
40. K. Moraki, S. Bengi, S. Zeyrek, M.M. Bülbül, Ş. Altındal, Temperature dependence of characteristic parameters of the Au/C₂₀H₁₂/n-Si Schottky barrier diodes (SBDs) in the wide temperature range. *J. Mat. Sci. Mat. Electron.* **28**, 3987–3996 (2017)
41. B.L. Sharma, *Metal-semiconductor Schottky Barrier junctions and their applications* (Plenum Press, New York, 1984)
42. M.A. Laurent, G. Gupta, D.J. Suntrup, S.P. DenBaars, Barrier height inhomogeneity and its impact on (Al, In, Ga) N Schottky diodes. *J. Appl. Phys.* **119**, 064501 (2016)
43. M.A. Mayimele, J.P.J. Rensburg, F.D. Aurret, M. Diale, Analysis of temperature-dependent current-voltage characteristics and extraction of series resistance in Pd/ZnO Schottky barrier diodes. *Phys. B* **480**, 58–62 (2016)
44. H. Tecimer, A. Türüt, H. Uslu, S. Altındal, I. Uslu, Temperature dependent current-transport mechanism in Au/(Zn-doped)PVA/n-GaAs Schottky barrier diodes (SBDs). *Sens. Actuat. A Phys.* **199**, 194–201 (2013)
45. F.A. Padovani, R. Stratton, Field and thermionic-field emission in Schottky barriers. *Solid State Electron.* **9**, 695 (1966)
46. J.P. Sullivan, R.T. Tung, M.R. Pinto, W.R. Graham, Electron transport of inhomogeneous Schottky barriers: a numerical study. *J. Appl. Phys.* **70**, 7403 (1991)
47. A.N. Saxena, Forward current-voltage characteristics of Schottky barriers on n-type silicon. *Surf. Sci.* **13**, 151–171 (1969)